

---

## Chapter 4

### Uniform global feedback — Experimental part

---

The following chapters of this work are devoted to the control of chemical turbulence and pattern formation in reaction-diffusion systems. Different approaches of control are discussed and applied to catalytic CO oxidation on Pt(110). This chapter is organized as follows. In Section 4.1, global control schemes are introduced. Their implementation into the experimental setup of catalytic CO oxidation is outlined and results from the application of external periodic forcing are given as an example. In Section 4.2, control of chemical turbulence by global delayed feedback is studied in experiments with catalytic CO oxidation. Finally, phenomena of spatiotemporal pattern formation in catalytic CO oxidation under global delayed feedback are presented in Section 4.3.

#### 4.1 Control techniques

Together with the study of self-organization in extended nonequilibrium systems, there came a growing interest in techniques to influence and control the space-time dynamics of such systems. Besides stabilization of unstable spatiotemporal states and the generation of novel complex patterns, the control of chaos in high-dimensional extended systems received much attention. Examples range from optical systems [76, 191], semiconductors [78, 192], and lasers [77, 193] to coupled map lattices [82, 194], chemical reaction-diffusion systems [79, 195], and coupled electrochemical oscillators [196]. Also in the context of the complex Ginzburg-Landau equation (CGLE), control of spatiotemporal chaos has been discussed [80, 81, 197, 198].

In general, control is established by introducing an additional force into the system. For a reaction-diffusion system the governing Eqs. (2.5) are then modified to

$$\partial_t \mathbf{u} = \mathbf{f}(\mathbf{u}, \mathbf{p}) + \mathbf{D}\nabla^2 \mathbf{u} + \mathbf{F}. \quad (4.1)$$

The force term  $\mathbf{F}$  can generally depend on space and time as well as on system variables and parameters. Different situations can be distinguished depending on the form of the term  $\mathbf{F}$ . Many control schemes involve *local* forcing where  $\mathbf{F}$  is space dependent. However, in practical applications, spatially resolved access to the individual system elements is often difficult to establish. Therefore, a *global* control is preferred in many experimental situations. In this case, the same force  $\mathbf{F}$  is applied independently of space at all locations of the system, *e.g.* by changing a global system parameter. Throughout this work, only global control schemes are discussed.

Commonly, control methods are further classified by considering whether the force  $\mathbf{F}$  depends on the dynamics of the system itself or not. If the control force is generated taking into account actual and/or past states of the system the control scheme is regarded as a *feedback*. If this is not the case and the term  $\mathbf{F}$  is defined independently of the behavior of the system the method is referred to as *external forcing*.

In the following, the implementation of global control into the experimental setup of catalytic CO oxidation on Pt(110) (see Section 2.2.5) will be discussed. Different global feedback schemes are introduced that are studied in more detail in later chapters of this work. In the second part of this section, results from the application of external periodic forcing to catalytic CO oxidation are presented as an example of pattern formation in a reaction-diffusion system under global control.

### 4.1.1 Implementation into the experimental setup

The experimental setup for catalytic CO oxidation that was discussed in Section 2.2.5 is extended to incorporate control schemes of both types, feedback and external forcing. In all cases discussed here, the control force acts on a global system parameter, the partial pressure of CO in the reactor. Since changes in the pressure are experienced equally at all locations on the catalyst surface, it is a globally implemented control.

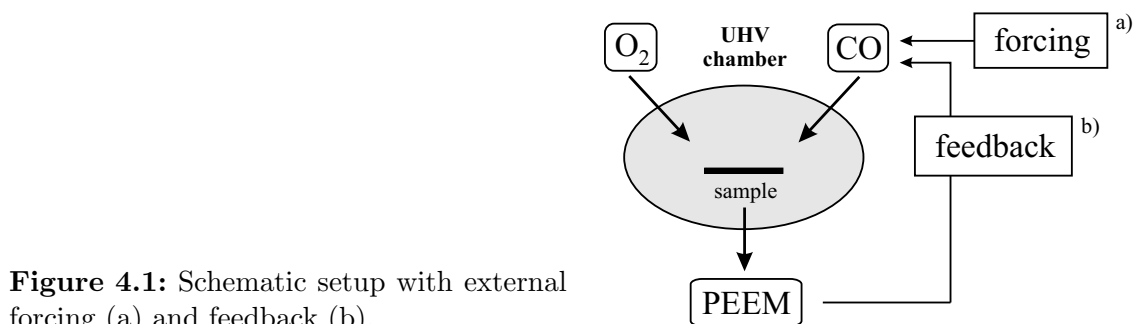


**Figure 4.1:** Schematic setup with external forcing (a) and feedback (b).

In the continuously pumped reaction chamber, the dosing rate of CO gas determines the CO partial pressure  $p_{\text{CO}}$  and is controlled by an automated gas inlet system. Changes in the electronic input signal of the inlet system induce modulations in the CO partial pressure that follow the input with an intrinsic delay of  $\tau_i \approx 0.6$  s determined by the residence time of gases in the pumped chamber. For periodically changing input signals frequencies up to 0.7 Hz with amplitudes up to 20% of the average  $p_{\text{CO}}$  level could be maintained (in all cases, the applied variations in CO partial pressure were large compared to pressure changes induced by global gas phase coupling).

A schematic setup including both external forcing (a) and feedback (b) is shown in Fig. 4.1. For external forcing, the dosing of CO is periodically modulated around a constant base level  $p_{\text{CO}}^0$  with an almost harmonic signal of amplitude  $\gamma$  and frequency  $\nu_f$ . Both amplitude and frequency of the forcing signal are control parameters that can be chosen independently. External periodic forcing and results from its application to catalytic CO oxidation are presented in the following section.

In the case of global feedback, the dosing rate of CO is linked to the spatiotemporal dynamics of concentration patterns on the catalytic surface by a feedback loop. In this work, two different situations are investigated. In the most basic setting, the CO supply is controlled by the intensity of the PEEM image, averaged over the entire observed area. This case is denoted as *uniform feedback* and will be discussed throughout most of the later chapters. In a first step towards more complex feedback schemes, *nonuniform feedback* will be introduced in the last chapter of this work. In order to generate a feedback signal from more specific properties of the concentration patterns, the instantaneous PEEM image is transformed to a frequency domain representation by Fast Fourier Transform (FFT) and the CO partial pressure is determined by the amplitude of selected modes from the frequency spectrum.

### 4.1.2 Example: External periodic forcing

In the remaining part of this section, the control of space-time dynamics in an extended oscillatory system is illustrated showing results from catalytic CO oxidation under external periodic forcing.<sup>1</sup> Periodic forcing is encountered in many different contexts related to phenomena as diverse as human heart beat, circadian rhythm, or tidal currents. Neglecting the spatial degrees of freedom, such systems can be considered as periodically forced nonlinear oscillators [21]. If driven by a frequency  $\nu_f$  different from its natural frequency  $\nu_0$ , the oscillator may become entrained to the external stimulus, a phenomenon commonly referred to as *frequency locking*. When locked to the stimulus, the system oscillates with a frequency  $\nu$  that is rationally related to the frequency of the external force,  $\frac{\nu_f}{\nu} = \frac{n}{m}$ . This general case of  $n : m$  resonance is denoted as subharmonic (superharmonic) if  $n > m$  ( $n < m$ ). Periodic forcing and entrainment of single oscillators is well understood and has been investigated in the context of many different systems, see *e.g.* Ref. [200] and references therein.

If a periodic force is applied to an extended system of diffusively coupled oscillators, the situation becomes more intricate. The diffusive coupling can enhance or suppress frequency locking [201]. Besides, different complex spatiotemporal phenomena can be observed. Experimental studies of periodically forced oscillatory reaction-diffusion systems were mostly performed using the light-sensitive Belousov-Zhabotinsky (BZ) reaction [38, 50, 51, 202]. A rich variety of space-time patterns could be stabilized, including phase clusters, stripe patterns, and labyrinthine structures. Theoretical efforts focused on the forced complex Ginzburg-Landau equation (CGLE) where instabilities and resonant pattern formation have been studied in great detail [53–55, 203].

**Catalytic CO oxidation under periodic forcing** The behavior of catalytic CO oxidation on Pt(110) under periodic forcing was already investigated shortly after self-sustained oscillations had been discovered in this reaction [204, 205]. Since spatially resolved techniques for the imaging of concentration distributions across the surface were not available at that time, observations were limited to temporal phenomena. Besides harmonic resonance, various bands of subharmonic and superharmonic entrain-

---

<sup>1</sup> The experiments on periodically forced catalytic CO oxidation reported here were performed in collaboration with Matthias Bertram [171, 199].

ment could be identified together with quasi-periodic behavior between the entrainment bands. The results presented here focus on the spatial patterns that can be observed in the CO oxidation system under external forcing.

The experimental system and the laboratory setup are explained in Section 2.2. Temperature and partial pressures are chosen such that the unperturbed system spontaneously develops chemical turbulence. External periodic forcing is implemented via the gas phase as explained above. Forcing frequencies in the range of  $0.20 \text{ Hz} \leq \nu_f \leq 0.67 \text{ Hz}$  are applied. To suppress turbulence and to induce frequency locked patterns, periodic modulations in CO partial pressure with a relative amplitude between 10% and 20% were necessary.

**Nonresonant patterns** For sufficiently strong forcing homogeneous oscillations could be established at all forcing frequencies. Below the transition to frequency locked uniform oscillations, two types of nonresonant patterns could be observed. On the one hand, when increasing the forcing amplitude from low values, freely evolving chemical turbulence was first replaced by *intermittent turbulence* characterized by the repeated emergence of bubble shaped objects on a uniformly oscillating background. They are randomly distributed across the imaged surface area and reproduce in cascades. On the other hand, starting from frequency locked uniform oscillations a cellular structure can emerge upon a decrease of the forcing strength. The arrays of cells arise as small modulations of the locked uniform oscillations and are visible only during a short interval of each oscillation cycle. Both patterns are discussed in detail elsewhere [171, 199]. They are similar to intermittent turbulence and cellular structures observed in the presence of global feedback, see Sections 4.3.2 and 4.3.3.

**Oscillatory stripes** Besides nonresonant structures, additional resonant patterns can be found at higher forcing frequency,  $\nu_f \geq 0.5 \text{ Hz}$ , due to 2:1 subharmonic entrainment of local oscillations. At the low frequency edge of this resonance, oscillatory stripes occur. The growth mechanism of this pattern is illustrated in the first five frames of Fig. 4.2 (a). Initially, the system performs small-amplitude uniform oscillations around a mainly CO covered state. At some locations on the surface, the oxygen covered state is occasionally reached. Starting from these points, the structure grows stripe by stripe until it occupies the entire imaged surface area. As time goes on, the number of dislocations in the pattern, *i.e.*, the regions where individual stripes merge to form a

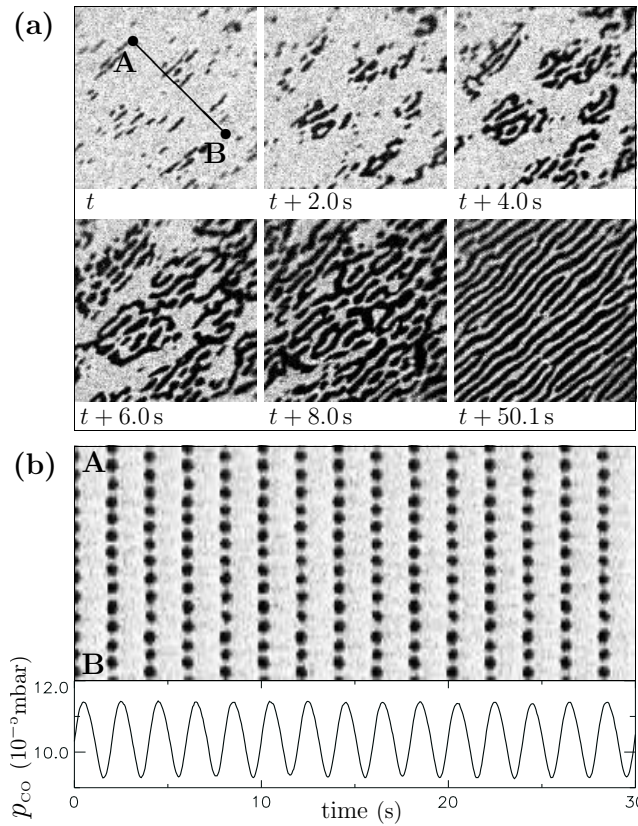


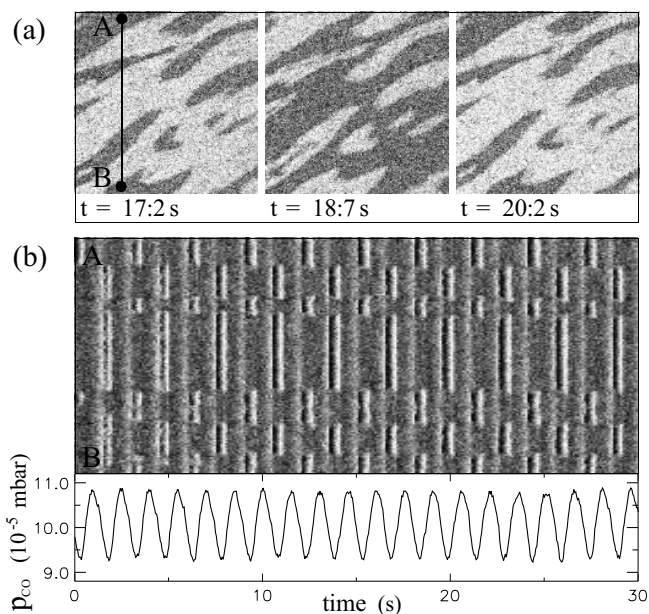
**Figure 4.2:** Irregular oscillatory stripes under periodic forcing. (a) PEEM images ( $240 \times 240 \mu\text{m}^2$ ) showing the initial development of the pattern at time intervals of one forcing period between subsequent snapshots (first five frames) and the fully developed structure (sixth frame). (b) Space-time diagram for the fully developed pattern, taken along the line  $AB$  indicated in the first image in (a). The curve below shows the corresponding temporal variation of CO partial pressure. The forcing frequency and amplitude are  $\nu_f = 0.50$  Hz and  $\gamma = 20.2\%$ , respectively. The parameters are  $T = 531$  K,  $p_{\text{O}_2} = 40.0 \times 10^{-5}$  mbar, and  $p_{\text{CO}}^0 = 10.4 \times 10^{-5}$  mbar [199].

fork-like junction, slowly decreases and a more regular, quasi-stationary configuration is established, see the sixth frame in Fig. 4.2 (a). Due to anisotropy of CO diffusion on the Pt(110) single crystal surface, the stripes are mainly oriented along the direction of fast CO diffusion (the  $[1\bar{1}0]$  direction).

In Fig. 4.2 (b), a space-time diagram of the fully developed stripe pattern is displayed taken along a cross-section perpendicular to the orientation of the stripes. The dark stripes occur only during relatively short intervals of each oscillation cycle as can be seen in this diagram. After one forcing period, the locations of stripes are shifted, so that new stripes appear between those seen during the previous cycle. Thus, the initial pattern is repeated every two forcing cycles. Local oscillations within the central regions of alternating stripes have the same shape and frequency ( $\nu = \nu_f/2$ ), but are shifted in time by one forcing period.

**Oscillatory phase clusters** At slightly higher forcing frequencies but still in the regime of the 2:1 subharmonic resonance, oscillatory cluster patterns can be induced at moderate forcing amplitudes. Upon the formation of phase clusters, the surface splits into

**Figure 4.3:** Phase clusters under periodic forcing. (a) Three snapshots ( $300 \times 300 \mu\text{m}^2$ ), separated by time intervals of one forcing period. (b) Space-time diagram taken along the line  $AB$  indicated in the first image in (a), and the corresponding temporal variation of CO partial pressure. The forcing frequency and amplitude are  $\nu_f = 0.67 \text{ Hz}$  and  $\gamma = 16.4 \%$ , respectively. The parameters are  $T = 523 \text{ K}$ ,  $p_{\text{O}_2} = 40.0 \times 10^{-5} \text{ mbar}$ , and  $p_{\text{CO}}^0 = 10.1 \times 10^{-5} \text{ mbar}$  [199].



large domains belonging to either of two dynamical states. Within both cluster states, local oscillations are entrained at half the frequency of the driving force,  $\nu = \nu_f/2$ . They are locked to the external stimulus with a phase shift of one forcing period between the two states. In contrast to oscillatory stripes, no intrinsic wavelength is found for phase clusters. An example of phase clusters is displayed in Fig. 4.3 (a), where three PEEM images are shown at time intervals of one forcing period between subsequent frames. After each period of the driving force, predominantly oxygen and CO covered regions have interchanged with respect to the previous PEEM image, so that the initial pattern is reestablished after two forcing cycles.

The temporal evolution of phase clusters is illustrated in a space-time diagram in Fig. 4.3 (b). Interfaces between domains of opposite phase are stationary and the spatial distribution of clusters is stable over several forcing periods. On a longer time scale, however, it was observed that phase clusters underwent sudden rearrangements after which a new spatial configuration of domains was established, which again was stable for a certain number of forcing periods.

**Frequency demodulation** Resonant patterns can be further analyzed employing a frequency demodulation technique that has been introduced to characterize similar data from BZ reaction experiments [50]. The temporal response at each point  $(x, y)$  is determined by Fourier transform of the time series at the respective pixel. For patterns

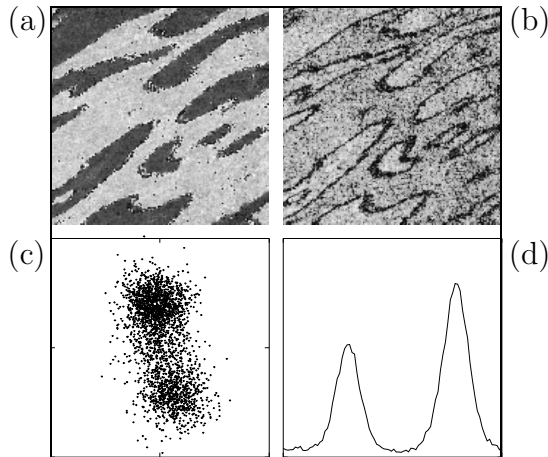


**Figure 4.4:** (a) Phase pattern, (b) amplitude pattern, (c) phase portrait, and (d) phase histogram for oscillatory phase clusters demodulated at frequency  $\nu_f/2$ . The parameters are as in Fig. 4.3 [199].

in the 2:1 subharmonic resonance, the power spectrum averaged over all pixels shows distinct peaks at the frequencies  $\nu_f$  and  $\nu_f/2$  (also higher harmonics are present). To obtain separate information on local amplitude and phase associated with the different excited temporal modes, the complex Fourier coefficients  $a(x, y)$  of the modes corresponding to the frequencies  $\nu_f$  and  $\nu_f/2$  are extracted from the frequency spectrum at each pixel. By plotting the spatial distributions of  $\arg(a)$  and  $|a|$ , phase and amplitude images can be obtained for the respective modes.

While phase and amplitude associated with the frequency  $\nu_f$  are uniformly distributed, the resonant pattern can be clearly seen for the subharmonic mode with frequency  $\nu_f/2$ . In Fig. 4.4, the results of a demodulation at the frequency  $\nu_f/2$  are shown for the phase clusters of Fig. 4.3. From the spatial distribution of  $\arg(a)$ , the different anti-phase domains can be clearly distinguished, see Fig. 4.4 (a). The oscillation amplitude (b) is strongly reduced at the domain interfaces while it is equally large within the cluster domains of opposite phase. The phase portrait (c) shows the Fourier coefficients of all pixels plotted into the complex plane. Two spots of accumulating points, corresponding to the pixels located within the anti-phase domains are obtained (the scattering of points is due to experimental noise). The points that connect these spots correspond to pixels located within the phase fronts. The histogram of phase angles is displayed in Fig. 4.4 (d). Obviously, the two phase states are not evenly weighted. The size ratio between the two peaks was different each time phase clusters were observed. Note that, in contrast to the situation here, phase clusters induced by global delayed feedback always show the property of phase balance as will be discussed in Section 4.3.3.

## 4.2 Controlling turbulence

Chemical turbulence in oscillatory reaction-diffusion systems can be controlled by application of appropriate global feedback. If turbulence is suppressed, regular spatiotemporal patterns may occur or, in the case of complete synchronization, uniform oscillations are established in the system. In the following, the stabilization of uniform oscillations is considered. More complex feedback induced patterns are presented in Section 4.3.

### 4.2.1 General remarks

The question of chaos control has first been addressed for low-dimensional systems in a work by Ott, Grebogi, and Yorke (OGY) [71]. Their work has inspired a large number of experimental and theoretical studies investigating the behavior of nonlinear dynamical systems under feedback control, see *e.g.* Refs. [72–74, 206–208]. The OGY method stabilizes unstable periodic orbits embedded in a chaotic attractor by applying small time-dependent perturbations. It is, however, restricted to relatively slow phenomena since permanent extensive computer analysis of the system state is required. In a much simpler algorithm proposed by Pyragas [75], continuous control of the system is established by a feedback signal, generated from the time series of one of the system variables. The applied feedback  $F$  is proportional to the difference between the delayed value of the chosen variable  $u$  and the instantaneous value of this variable,  $F \sim u(t - \tau) - u(t)$ . This scheme is often referred to as *time-delay autosynchronization* (TDAS) [209]. In previous work, the application of TDAS has been studied, either experimentally or theoretically, for only a few systems such as lasers [77], semiconductors [78], glow discharge devices [210], and populations of electrochemical oscillators [211]. Extensions [212] and considerable improvements [192, 213] of TDAS were reported in recent literature. For spatially extended experimental systems that do not allow local access to their individual elements, TDAS can be applied as a global feedback, where the control signal is generated from the integral value of  $u$  over all system elements.

In catalytic CO oxidation on Pt(110), suppression of spatiotemporal chaos by global feedback was qualitatively demonstrated in a recent work [79]. In the present study, the TDAS feedback scheme is applied to the CO oxidation system, in order to investigate

control of turbulence in more detail, in particular, with respect to the invasiveness of the control scheme. The experimental setup is described in Section 2.2.5 and the feedback is implemented globally via the gas phase as explained in Section 4.1.1. The control signal is generated in the following way. The integral intensity  $I(t)$  of the PEEM image is continuously recorded, normalized between zero and unity for the completely O and CO covered surface, respectively. From this quantity, the feedback signal is computed by taking the difference between the instantaneous integral image intensity and the intensity delayed by a chosen delay time  $\tau$ . This signal, multiplied by an additional intensity factor  $\mu$ , is used as input for the electronically operated dosing system of CO gas to the reaction chamber. The CO partial pressure inside the chamber was thus modulated according to

$$p_{\text{CO}}(t) = p_{\text{CO}}^0 + \mu(I(t - \tau) - I(t)). \quad (4.2)$$

Note that an additional control loop latency  $\tau_i$  is present, due to the finite pumping rate of the chamber. In Section 5.1.2, the effect of a control loop latency  $\tau_i$  was investigated in numerical simulations using a standard realistic model of catalytic CO oxidation on Pt(110). For  $\tau_i \ll \tau$  there was no significant qualitative difference to the results without control loop latency and, therefore, the effect of an intrinsic delay was neglected in the discussion of the results.

Below, a series of experiments is presented, where both the feedback intensity  $\mu$  and the delay time  $\tau$  in the feedback scheme (4.2) are varied. Temperature and partial pressures of the reactants are chosen such that in absence of feedback, homogeneous oscillations are unstable and the system spontaneously develops a state of highly irregular spiral-wave turbulence. A snapshot of this state is shown in Fig. 4.5 (a).

### 4.2.2 Transition to complete synchronization

In the presence of feedback, the system gradually synchronizes with increasing feedback intensity  $\mu$ . An example of the feedback-induced transition from turbulence to homogeneous oscillations is shown in Fig. 4.5. The upper part displays a sequence of three PEEM images. For zero feedback intensity, the system is in a state of fully de-

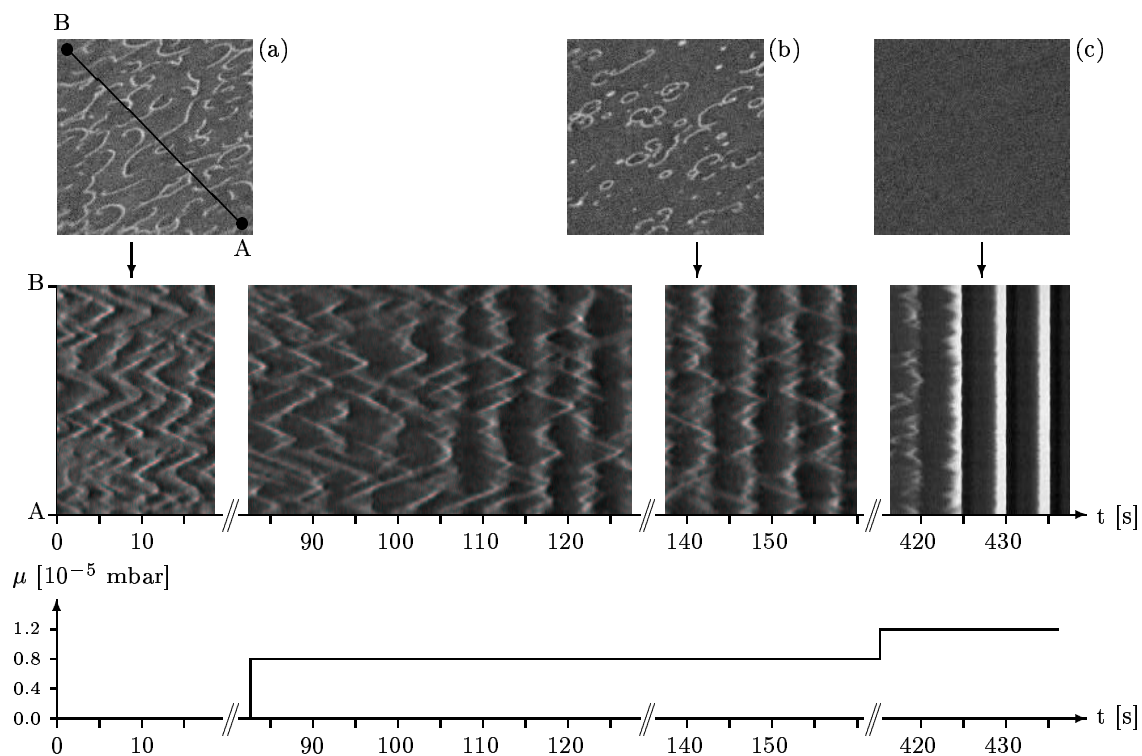


**Figure 4.5:** Feedback-induced transition from chemical turbulence to homogeneous oscillations. (top, a) Snapshots of freely developing chemical turbulence in absence of feedback, (b) intermittent turbulence for small values of feedback intensity, and (c) homogeneous oscillations for higher values of feedback intensity. (middle) Space-time plot for the transition from turbulence to homogeneous oscillations along the line AB indicated in image (a). From left to right, the plot shows, with increasing time, turbulence for  $\mu = 0.0$ , transition to intermittent turbulence and the persistent state of intermittent turbulence for  $\mu = 0.77 \times 10^{-5}$  mbar, and the transition to homogeneous oscillations for  $\mu = 1.2 \times 10^{-5}$  mbar. Below the space-time diagram, the feedback intensity is plotted as a function of time. The parameters are  $T = 505$  K,  $p_{\text{O}_2} = 4 \times 10^{-4}$  mbar,  $p_{\text{CO}}^0 = 9.5 \times 10^{-5}$  mbar, and  $\tau = 3$  s [95].

veloped spiral-wave turbulence as displayed in Fig. 4.5 (a). There are no long living coherent patterns and the turbulent state is characterized by small irregular rotating spiral-wave fragments that continuously move and break up. These waves emerge randomly and, upon meeting each other, undergo mutual annihilation. For intermediate values of  $\mu$ , oscillations are already synchronized to a certain extent and a state of intermittent turbulence is observed similar to the regime described in the next section, cf. Fig. 4.5 (b) and Fig. 4.8. In the experiment presented here, intermittent turbulence is dominated by localized, repeatedly breaking spiral fragments on an almost uniformly oscillating background. Bubble-like structures may also be observed. However, in most

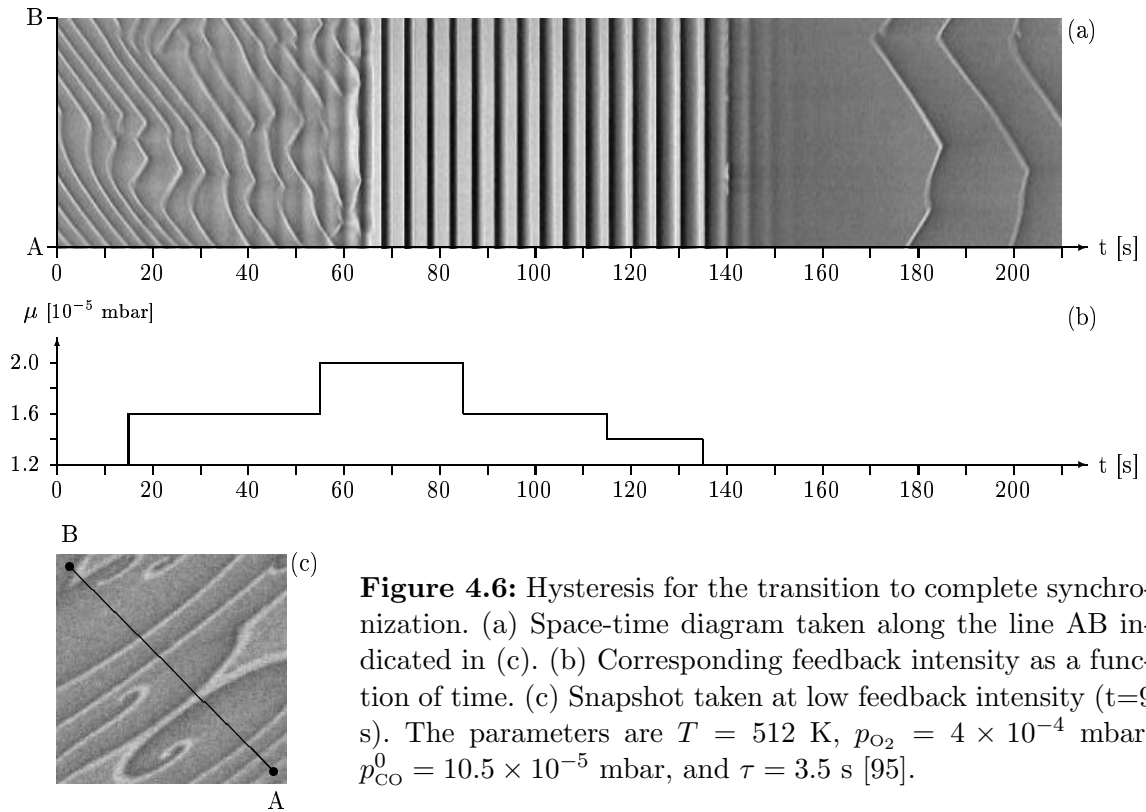


**Figure 4.6:** Hysteresis for the transition to complete synchronization. (a) Space-time diagram taken along the line AB indicated in (c). (b) Corresponding feedback intensity as a function of time. (c) Snapshot taken at low feedback intensity ( $t=9$  s). The parameters are  $T = 512$  K,  $p_{\text{O}_2} = 4 \times 10^{-4}$  mbar,  $p_{\text{CO}}^0 = 10.5 \times 10^{-5}$  mbar, and  $\tau = 3.5$  s [95].

cases they burst and undergo breakups, forming again irregular spiral-wave fragments. Finally, for higher feedback intensities, complete synchronization is reached and the system performs homogeneous oscillations, see Fig. 4.5 (c).

The space-time plot in the middle part of Fig. 4.5 further illustrates the process of synchronization. The plot is taken along the diagonal of the PEEM images from the top left to the bottom right hand corner, corresponding roughly to the [001] direction along which surface diffusion of CO is slow. The feedback intensity  $\mu$  is increased in the course of time (see the graph at the bottom of Fig. 4.5). The first part from the left (0 to 18 s) shows a space-time plot for the turbulent state of the system in absence of feedback. The second part (from 82 s onwards) illustrates the transient from turbulence to intermittent turbulence and the third part (137 to 160 s) gives a space-time plot of the state of intermittent turbulence, where oscillations are already partly synchronized. Finally, after a short transient, the completely synchronized state of homogeneous oscillations is reached (416 to 437 s).

### 4.2.3 Hysteresis

For synchronization of the system in dependence on the feedback intensity  $\mu$ , strong hysteresis effects are observed. In Fig. 4.6 (a), the space-time diagram of an experiment is shown, where the feedback intensity is increased until homogeneous oscillations are reached and subsequently decreased again until synchronization is lost and patterns start to evolve. In this experiment, the parameters are chosen such that the initial state of the system in absence of feedback is less turbulent and shows evolving and interacting waves and large spiral fragments. A snapshot of this state is displayed in Fig. 4.6 (c). As shown in Fig. 4.6 (b), the feedback intensity is increased from  $\mu = 1.2 \times 10^{-5}$  mbar to  $\mu = 2.0 \times 10^{-5}$  mbar and then decreased again to  $\mu = 1.2 \times 10^{-5}$  mbar in the course of time. Obviously, coming from the uncontrolled state, the feedback intensity needed to synchronize the system is much higher than the feedback intensity necessary to maintain homogeneous oscillations when starting from the state of complete synchronization and decreasing the feedback intensity. When synchronization is lost at low feedback intensity, the wavelength of the patterns which start to evolve is, at first, much longer than it was at the beginning of the experiment. However, it decreases with time and soon the system reaches its initial state again (not shown in Fig. 4.6).

### 4.2.4 Period versus delay

In the state of control, the period  $T$  of homogeneous oscillations depends on the choice of the delay time  $\tau$  in the feedback scheme. In Fig. 4.7, the period  $T$  is plotted as a function of the delay time  $\tau$  (black squares). A series of experiments was performed to obtain this plot. At the beginning of each experiment, the CO supply was kept closed and only oxygen was present in the reaction chamber, causing a uniform oxygen coverage on the sample surface. At  $t = 0$ , the CO valve was opened to its predefined value. The parameters were chosen such that, in the absence of feedback, chemical turbulence would spontaneously develop. In these experiments, however, the feedback intensity factor  $\mu$  was chosen large enough to prevent the emergence of turbulence and to stabilize homogeneous oscillations. The oscillation period was then determined for different values of the delay time  $\tau$ .

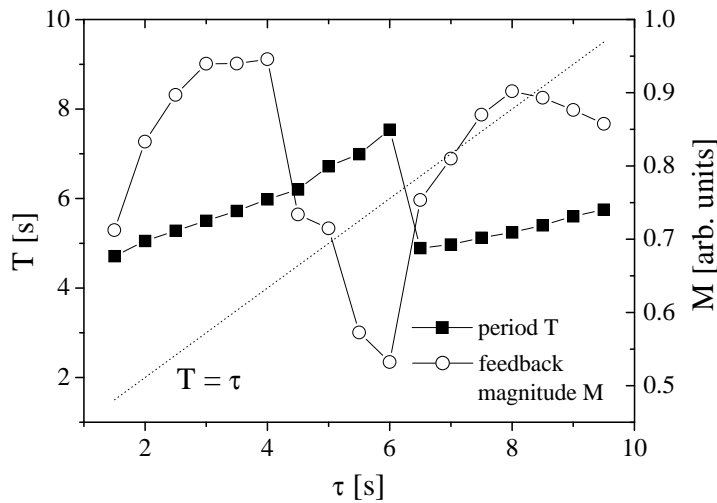


**Figure 4.7:** Period  $T$  of homogeneous oscillations (black squares) and feedback magnitude  $M$  (open circles) as function of the delay time  $\tau$ . The parameters are  $T = 515$  K,  $p_{\text{O}_2} = 4 \times 10^{-4}$  mbar,  $p_{\text{CO}}^0 = 10.0 \times 10^{-5}$  mbar, and  $\mu/p_{\text{CO}}^0 = 0.32$  [95].

Superposed in the same diagram, the strength of the feedback signal acting on the system at different delay times is displayed. To measure the impact of the feedback, the value of  $M = \langle |I(t - \tau) - I(t)| \rangle$  is plotted, which is the time average over the modulus of the feedback signal (open circles in Fig. 4.7). The quantity  $M$  is called the *feedback magnitude*. Since the feedback signal is oscillating around zero, the feedback magnitude is computed as the time-average of the modulus of the feedback signal. Thus, this quantity is a measure for the absolute average driving force that is imposed on the system by the feedback and hence quantifies the invasiveness of the feedback. Finally, the line given by  $T = \tau$  is displayed. For each point on this line, the feedback signal vanishes, as can be easily seen from Eq. (4.2). Thus, these points represent the optimal case of a noninvasive feedback.

The experimental results show that the period of uniform oscillations approaches the line where  $T$  equals  $\tau$  with increasing delay. However, the actual intersection point for which  $T = \tau$  was not reached in the experiments. Instead, a jump occurred around the line given by  $T = \tau$  and the system evades the point where its oscillation period would become equal to the delay time. Thus, as the value of  $T$  approaches  $\tau$ , the feedback magnitude could be decreased by about 50%, indicating that the invasiveness of the feedback can be reduced considerably by optimizing the choice of the delay time in the feedback scheme. However, a feedback signal that vanishes in the state of control could be expected only if uniform oscillations with  $T = \tau$  were stabilized. This optimal case of completely noninvasive control could not be established in the experiments.

For understanding and interpretation of the experimental observations, the feedback induced behavior is analyzed theoretically in terms of general models of oscillatory systems. Theoretical arguments and numerical simulations of a phase dynamics model and the complex Ginzburg-Landau equation are presented in Chapter 5.

## 4.3 Spatiotemporal pattern formation

In the previous section, it was demonstrated that chemical turbulence in catalytic CO oxidation on Pt(110) can be suppressed by application of sufficiently strong global delayed feedback. In a narrow interval of intermediate feedback intensities close to the transition from turbulence to uniform oscillations, different spatiotemporal patterns can be stabilized. In this section, an overview of the experimentally observed complex space-time patterns in the CO oxidation system under global delayed feedback is presented.<sup>2</sup>

Similar experiments have been conducted before applying global feedback in a parameter regime where the freely evolving reaction does not show chemical turbulence [215]. Besides, pattern formation under global delayed feedback was intensively studied in the framework of a realistic model of catalytic CO oxidation on Pt(110). Numerical simulations under both turbulent and nonturbulent conditions were performed and discussed in detail [57, 171, 216]. Pattern formation under global feedback was also studied in the context of the oscillatory BZ reaction in experiments as well as model simulations [39, 52, 56].

### 4.3.1 General remarks

For the experiments presented here, a feedback protocol slightly different from the TDAS scheme was employed. The CO partial pressure in the chamber was controlled according to the following relation,

$$p_{\text{CO}}(t) = p_{\text{CO}}^0 + \mu (I(t - \tau) - I_{\text{ref}}). \quad (4.3)$$

Again,  $I(t)$  denotes the instantaneous spatially averaged intensity of the PEEM image, scaled between zero and unity for the O and CO covered surface, respectively. The constant reference value  $I_{\text{ref}}$  was determined prior to each series of experiments as the time average of the global PEEM intensity  $I(t)$  in the initially developing state of spiral-wave turbulence. Also in the feedback scheme (4.3), delay time and a feedback

---

<sup>2</sup> The experiments were performed in collaboration with Matthias Bertram [171, 214].

intensity factor are independently chosen control parameters. In this case, however, the effective time delay  $\tau$  simply constitutes the sum of the intrinsic delay  $\tau_i$  and the externally chosen time lag.

A large number of experiments was conducted to study the spatiotemporal dynamics of the system under systematic variation of the feedback parameters  $\mu$  and  $\tau$ . In the beginning of each series of experiments, partial pressures and temperature were chosen such that the reaction was oscillatory and, furthermore, chemical turbulence spontaneously developed in absence of feedback. For sufficiently strong feedback intensities  $\mu$  turbulence could be suppressed and turned into stable uniform oscillations at any delay time  $\tau$  (delays up to  $\tau = 10$  s have been investigated). Generally, complete synchronization could be reached with feedback induced changes in CO partial pressure of about 5% of the CO pressure base level  $p_{\text{CO}}^0$ . However, at some delays, higher feedback intensities were necessary, corresponding to CO partial pressure variations of up to 20% in the state of synchronous oscillations. The period of uniform oscillations was affected by the feedback and varied approximately between 3 s and 10 s, with a tendency to increase for longer delays and decrease for stronger feedbacks. For feedback intensities below the threshold of complete synchrony, a variety of space-time patterns emerge that will be discussed in the following. In general, strong hysteresis is present at the transition from the regime of spatiotemporal pattern formation to uniform oscillations, that is, at a fixed time delay, uniform oscillation disappear at significantly smaller feedback intensities upon a decrease of  $\mu$  than they appear if  $\mu$  is increased from lower values.

### 4.3.2 Intermittent turbulence

As the feedback intensity is increased starting from zero, turbulent spiral waves are first replaced by intermittent turbulence for any choice of the delay time  $\tau$ . Intermittent turbulence is characterized by turbulent cascades of localized patterns on a uniformly oscillating background. Two types of such objects can be identified, namely bubble-shaped structures and spiral-wave fragments. An example of the first type of intermittent turbulence is displayed in Fig. 4.8 (a)–(c). The snapshots in Fig. 4.8 (a) illustrate one evolution cycle of the pattern. Starting from a dark, uniformly covered state, bright spots appear at different locations. As these objects grow beyond a cer-

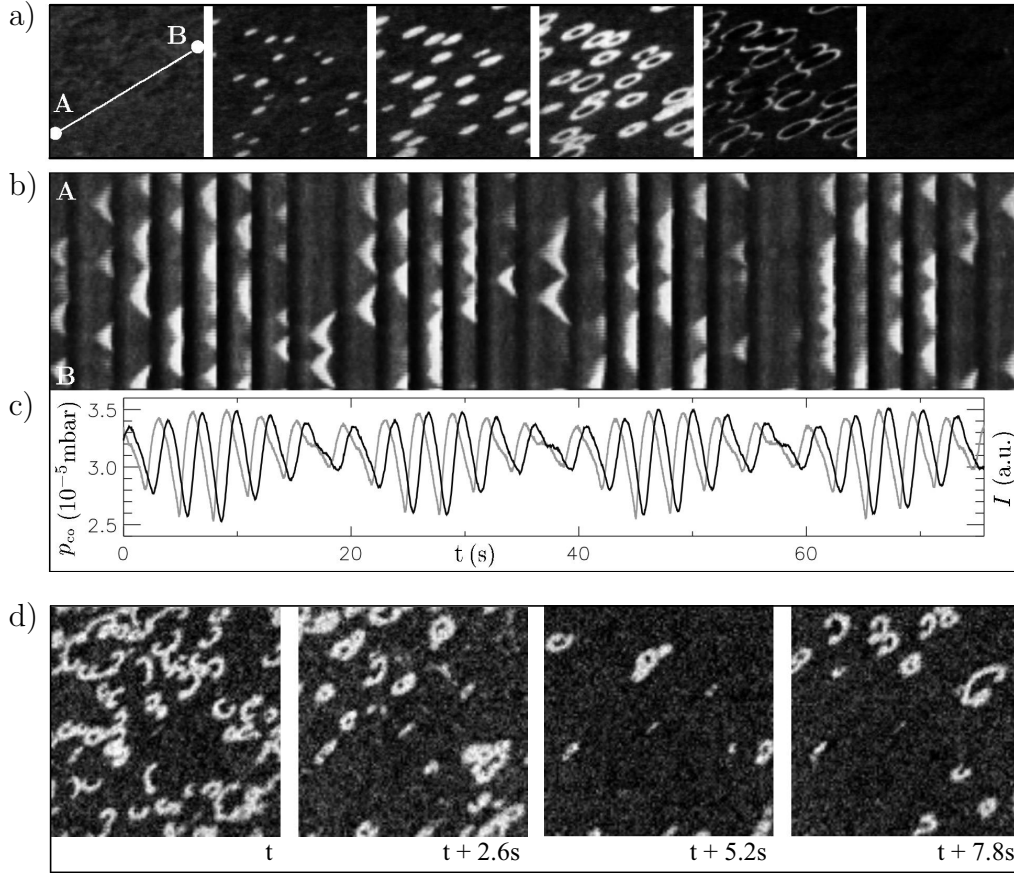


**Figure 4.8:** Intermittent turbulence. (a) Six subsequent snapshots ( $360 \times 360 \mu\text{m}^2$ ) showing the evolution of bubble structures, taken at intervals of  $\Delta t = 0.7$  s during one oscillation period. (b) Space-time diagram along the line  $AB$  indicated in the first frame in (a). (c) Temporal variations of CO partial pressure (black line) and integral PEEM intensity (gray line). (d) PEEM images ( $330 \times 330 \mu\text{m}^2$ ) of intermittent turbulence showing localized spiral fragments. The parameters are (a)–(c)  $T = 495$  K,  $p_{\text{O}_2} = 10.0 \times 10^{-5}$  mbar,  $p_{\text{CO}}^0 = 3.15 \times 10^{-5}$  mbar,  $\mu = 2.0 \times 10^{-5}$  mbar, and  $\tau = 0.8$  s; (d)  $T = 537$  K,  $p_{\text{O}_2} = 40.0 \times 10^{-5}$  mbar,  $p_{\text{CO}}^0 = 11.4 \times 10^{-5}$  mbar,  $\mu = 3.0 \times 10^{-5}$  mbar, and  $\tau = 0.7$  s [214].

tain size, darker regions start to develop inside, transforming them into ring-shaped structures. These dark regions expand rapidly and after some time the whole pattern fades away and is replaced by the uniform dark state. Then the entire cycle repeats. In Fig. 4.8 (b), a space-time diagram is displayed taken along the line  $AB$  indicated in the first frame in (a). Expanding bubbles are represented by triangular structures in the cross section. Obviously, bubbles can die and reproduce. Analyzing the evolution of the pattern over many oscillation periods, a cyclic behavior of repeated reproduction cascades is observed. Bubbles reproduce until many of them are present, covering al-

most the entire imaged surface. Then, sudden annihilation occurs, so that only a few of them survive and start to reproduce again. In the example shown, these reproduction cycles take place on a time scale of about six oscillation periods. During intermittent turbulence, the CO partial pressure shows aperiodic variations but is rigidly correlated with the evolution cycles of the pattern as can be seen in Fig. 4.8 (c). Here, the temporal variations of CO pressure (black line) and the integral PEEM intensity (gray line) are displayed.

A similar state of intermittent turbulence can be observed which is composed of localized spiral wave fragments instead of bubble structures. This state predominantly occurred at higher values of temperature, where chemical turbulence is highly irregular, displaying many small spiral fragments. Typical PEEM images of intermittent turbulence where spiral wave fragments appear on a background of uniform oscillations are displayed in Fig. 4.8 (d).

### 4.3.3 Regular patterns

Besides intermittent turbulence, several regular space-time patterns can be observed. Depending on the choice of feedback parameters, *standing waves*, *cellular structures*, and *cluster patterns* could be stabilized. They were observed for delays in the interval  $0.6 \text{ s} < \tau < 1.0 \text{ s}$ . The precise stability regions of these patterns sensitively depend on the choice of temperature and partial pressures.

**Standing waves** Oscillatory standing waves are characterized by the repeated appearance of alternating bright and dark stripes from a uniform state. They form a spatially periodic array and have a wavelength of roughly  $20 - 50 \mu\text{m}$  depending on the choice of parameters. Due to anisotropy of CO diffusion on the Pt(110) single crystal facet, the stripes are mainly oriented along the direction of fast CO diffusion (the  $[1\bar{1}0]$  direction). The stripes are visible only during relatively short intervals of each oscillation cycle and appear at the transitions between uniformly dark and bright states. A typical example of oscillatory standing waves is displayed in Fig. 4.9 (a), where four snapshots taken in the course of one oscillation cycle are shown. From the space-time diagram in Fig. 4.9 (b) it becomes obvious that the locations of stripes during subse-

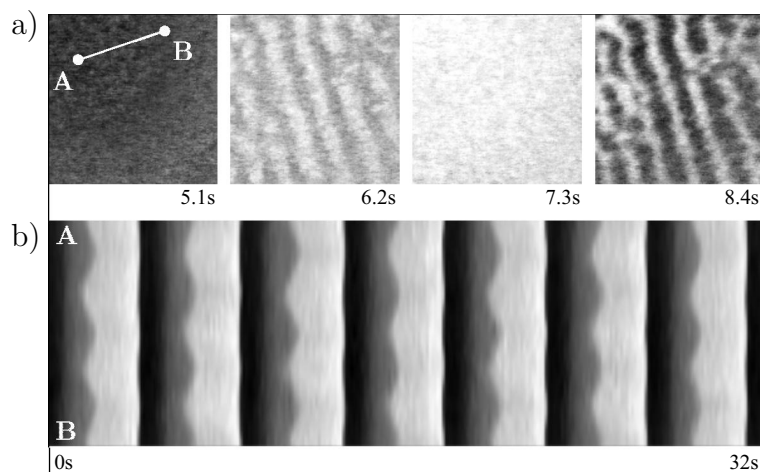


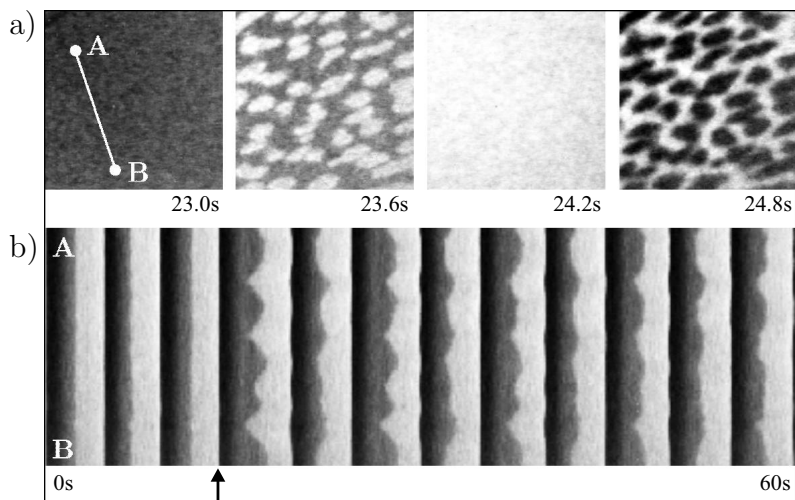
**Figure 4.9:** Standing wave pattern. (a) Four subsequent PEEM images ( $270 \times 270 \mu\text{m}^2$ ) taken during one oscillation period. (b) Evolution along the line  $AB$  indicated in (a). Parameters:  $T = 505 \text{ K}$ ,  $p_{\text{O}_2} = 10.0 \times 10^{-5} \text{ mbar}$ ,  $p_{\text{CO}}^0 = 3.30 \times 10^{-5} \text{ mbar}$ ,  $\mu = 1.6 \times 10^{-5} \text{ mbar}$ , and  $\tau = 0.8 \text{ s}$  [214].

quent oscillation cycles are shifted, so that bright stripes appear where dark ones have been before and vice versa. Thus, the initial pattern is repeated after two periods of local oscillations.

Similar standing wave patterns have been reported previously in catalytic CO oxidation on Pt(110) without global delayed feedback [46, 134]. In these earlier experiments, most of the catalyst surface remained in a state of uniform oscillations and standing waves were observed only on parts of the surface. Therefore, they were attributed to the stabilizing effect of an intrinsic periodic force that was generated by the large fraction of uniformly oscillating surface and transported through global gas phase coupling [134]. In numerical simulations, they could be reproduced only when a subsurface oxygen species was taken into account [134]. It is therefore assumed that small amounts of subsurface oxygen might also be involved in the present experiments.

**Cellular structures** Similar to standing waves, oscillatory arrays of cells occupy the entire imaged surface area and are visible only during short intervals within each oscillation period when the surface switches between the uniformly CO and O covered states. One oscillation cycle sampled by four subsequent snapshots is displayed in Fig. 4.10 (a). Typically, the cellular arrays have an irregular structure with an average cell size of approximately  $20 \mu\text{m}$ . No unambiguously regular, hexagonal arrays have been observed. In the present experiment, cellular structures were generated from a standing wave pattern upon a slight decrease of the feedback intensity. This process is illustrated in Fig. 4.10 (b) in a space-time diagram, where the black arrow indicates the sudden decrease in  $\mu$  at  $t = 14 \text{ s}$  (the initial standing waves are not seen because

**Figure 4.10:** Cellular structures. (a) Four subsequent PEEM images ( $270 \times 270 \mu\text{m}^2$ ) taken during one oscillation period. (b) Space-time diagram along the line  $AB$  indicated in (a). The arrow indicates the time where  $\mu$  was reduced from  $1.6 \times 10^{-5}$  mbar to  $1.1 \times 10^{-5}$  mbar. Other parameters were as in Fig. 4.9 [214].



the cross section for the space-time plot is chosen parallel to the orientation of the stripes). In earlier work, cellular structures of a much smaller length scale were seen at lower temperatures using mirror electron microscopy [137].

**Oscillatory clusters** In the state of oscillatory phase clusters, the surface is divided into large domains (“clusters”) of synchronous oscillations. Two oscillatory states can be distinguished that show the same period and amplitude while their phases are shifted by half a period with respect to each other. In general, several domains develop, each belonging to one of the two anti-phase states. No intrinsic spatial wavelength is found in such a pattern. In Fig. 4.11 (a), snapshots of phase clusters are shown at time intervals of half an oscillation period apart. Between neighboring frames, CO and O covered regions have approximately interchanged, while after a full period (every second image) the spatial distribution of the different domains is repeated. This is also seen in the space-time diagram in Fig. 4.11 (b) showing the temporal evolution along the cross section  $AB$  indicated in the first frame of (a). The boundaries of the cluster domains perform a slight breathing variation. However, on longer time scales, the locations of domain interfaces are almost stationary or undergo only a weak drift. To further analyze the oscillatory states, Fig. 4.11 (c) displays the temporal variations of the PEEM intensity at two points within cluster domains of opposite phase (the positions of the sample points are indicated by arrows to the left of the space-time diagram). The intensity curves clearly reflect period-two oscillations as both curves exhibit alternating strong and weak maxima. The local oscillation period is about twice the period of uniform oscillations occurring at a slightly increased feedback intensity.

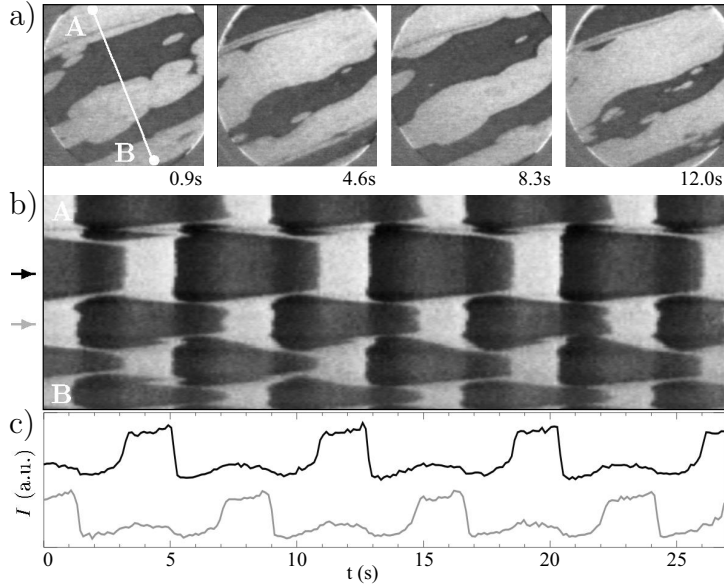


**Figure 4.11:** Oscillatory phase clusters. (a) Four subsequent PEEM images ( $500\ \mu\text{m}$  in diameter). (b) Space-time diagram along the line  $AB$  indicated in (a). (c) Variation of the local PEEM intensity at two different points indicated by the arrows in (b). Parameters:  $T = 500\ \text{K}$ ,  $p_{\text{O}_2} = 10.0 \times 10^{-5}\ \text{mbar}$ ,  $p_{\text{CO}}^0 = 3.07 \times 10^{-5}\ \text{mbar}$ ,  $\mu = 0.6 \times 10^{-5}\ \text{mbar}$ , and  $\tau = 0.8\ \text{s}$  [214].

Besides, at the domain interface, the difference between the two maxima is strongly reduced so that oscillations become almost simple periodic and have an intermediate amplitude. Note that oscillatory phase clusters under global delayed feedback fulfill the condition of *phase balance*. This means that the total areas occupied by the two anti-phase domains within the feedback window are approximately equal.

#### 4.3.4 Varying size of the feedback window

In a further set of experiments, the effect of a changed size of the feedback window on the formation of patterns was investigated. The experimental setting remained the same, except for the difference that the integral intensity value  $I(t)$  was not computed from the entire imaged surface area but from a small rectangular region of size  $250 \times 180\ \mu\text{m}^2$  in the lower half of the PEEM window. For appropriate choices of feedback parameters space-time structures similar to the above described patterns could be stabilized. No significant qualitative differences between the patterns that formed inside and outside the feedback window were observed. However, for oscillatory phase clusters a substantial difference was found in the modified setup. In Fig. 4.12 (a), a snapshot of a typical cluster pattern is shown. The region that was used for generation of the control signal is indicated by a rectangular box. As in the previous investigations, oscillations within the different cluster domains are shifted by half a period and

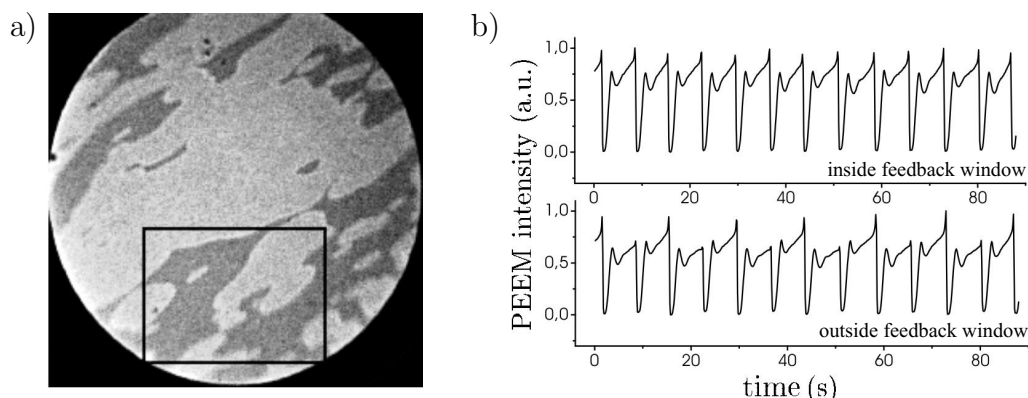


**Figure 4.12:** Feedback window of reduced size. (a) Snapshot of phase clusters with feedback window indicated by the rectangular box. (b) Temporal evolution of the integral PEEM intensity inside (upper curve) and outside (lower curve) of the feedback window. The parameters are  $T = 524$  K,  $p_{\text{O}_2} = 10.0 \times 10^{-5}$  mbar,  $p_{\text{CO}}^0 = 3.10 \times 10^{-5}$  mbar,  $\mu = 3.3 \times 10^{-5}$  mbar, and  $\tau = 0.75$  s [214].

local oscillations exhibit a clear period-two behavior. However, in the present experiment, clusters showed the property of phase balance only within the reduced feedback window, while the total size of the different phase domains over the entire monitored surface area was generally not balanced. This becomes evident when the overall oscillations of the image intensity within the feedback window and for the region outside the feedback window are followed in the course of time, see Fig. 4.12 (b). Inside the feedback window, the evenly weighted contributions of the oscillating anti-phase domains sum up to a periodic global signal of twice the frequency of local oscillations. In contrast, the contributions of the anti-phase clusters to the global intensity oscillations are not balanced outside the rectangular region and, thus, oscillations of the integral intensity are of period-two type and have a twice larger period. The lack of phase balance outside the feedback window can be understood from the following considerations. Inside the feedback window, a closed feedback loop acts on the patterns maintaining phase balance. The patterns outside this region are subject to an external force generated independently from a different region of the system (within the feedback window). Therefore, shape and size of the phase domains outside the feedback window are determined only by the local initial conditions prior to the application of feedback.

